

Cyclotron quantization and mirror-time transition on nonreciprocal lattices

Kai Shao,¹ Zhuo-Ting Cai,¹ Hao Geng,¹ Wei Chen,^{1,*} and D. Y. Xing¹

¹National Laboratory of Solid State Microstructures, School of Physics,
and Collaborative Innovation Center of Advanced Microstructures, Nanjing University, Nanjing 210093, China
(Dated: August 10, 2022)

Unidirectional transport and localized cyclotron motion are two opposite physical phenomena. Here, we study the interplay effects between them on nonreciprocal lattices subject to a magnetic field. We show that, in the long-wavelength limit, the trajectories of the wave packets always form closed orbits in four-dimensional (4D) complex space. Therefore, the semiclassical quantization rules persist despite the nonreciprocity, which preserves real Landau levels. We predict a different type of non-Hermitian spectral transition induced by the spontaneous breaking of the combined mirror-time reversal (\mathcal{MT}) symmetry, which generally exists in such systems. An order parameter is proposed to describe the \mathcal{MT} phase transition, not only to determine the \mathcal{MT} phase boundary but also to quantify the degree of \mathcal{MT} -symmetry breaking. Such an order parameter can be generally applied to all types of non-Hermitian phase transitions.

Introduction.-Non-Hermitian physics [1–3] has attracted growing research interest recently for its intriguing properties and potential applications that can be implemented in various physical systems, including photonic systems [4–9], open quantum systems coupled to the environment [10–13], quasiparticles in condensed matter [14–17], and electrical circuits [18–22]. The non-Hermitian topological band theory has been studied extensively and achieved plentiful results [23, 24], such as anomalous edge modes [25, 26], enriched topological phases [27–30], and topological lasing [31–33]. It is now well accepted that the conventional Bloch band theory should be replaced by the non-Bloch band theory for non-Hermitian systems with the so-called non-Hermitian skin effect (NHSE) [34, 35].

The NHSE is a unique phenomenon [34–41] meaning that all the bulk states are driven to the edge of the system under the open boundary condition (OBC), which has been confirmed in recent experiments in various physical systems [42–48]. Its intriguing interplay with the parity-time (\mathcal{PT}) phase transition has attracted attentions very recently [49–52], which opened up the possibility of manipulating the \mathcal{PT} transition by the NHSE. Physically, the NHSE in one-dimensional (1D) systems originates from the point gap topology of the energy spectra under the periodic boundary condition (PBC) [37–39], which is manifested as the nonreciprocal propagation of the wave packet through the system [53, 54]. Such nonreciprocity as shown in Figs. 1(a) and (b) is a particular type of delocalization effect and can induce a delocalization transition [55–57].

In contrast to nonreciprocal propagation, a magnetic field in a 2D system leads to the opposite effect. The motion of charged particles in a magnetic field forms cyclotron orbits with the guiding centers localized in space; see Fig. 1(e). The quantization of these cyclotron orbits results in flat Landau bands with zero mobility, which is incompatible with the picture of nonreciprocal propagation. Given that a magnetic field and nonreciprocity may

coexist in a variety of natural and artificial systems [58–61], it is interesting to explore their fascinating interplay and the resultant physical effects. Open questions that naturally arise include the robustness of cyclotron orbits as well as their quantization against nonreciprocity and possible new types of non-Hermitian phase transitions, etc.

In this Letter, we study the physical effects in nonreciprocal systems subject to a magnetic field. We show that semiclassical trajectories of the wave packets always form closed orbits in the 4D complex space in the long-wavelength limit despite the nonreciprocity. As a result, the Onsager-Lifshitz quantization rule persists, which protects real Landau levels from being complex. Moreover, we show that such non-Hermitian magnetic systems generally possess an inherent mirror-time reversal (\mathcal{MT}) symmetry, which dictates a spectral phase transition, dubbed the \mathcal{MT} transition. Specifically, a real-to-complex spectral transition occurs along with the spontaneous breaking of the \mathcal{MT} symmetry. An order parameter is proposed to quantify the \mathcal{MT} -symmetry breaking, which not only gives a definite phase boundary but also specifies to what extent the symmetry is broken. Our work generalizes the celebrated \mathcal{PT} physics [7–9] to the \mathcal{MT} scenario in a class of magnetic systems, which may lead to interesting observations and applications.

Model.-To be concrete, we first study the nonreciprocal square lattice in Fig. 1(a) and then verify the universality of the results on the honeycomb lattice in Fig. 1(b). A square lattice with nonreciprocal hopping under a magnetic field B can be described by the modified Harper-Hofstadter model as [62, 63]

$$H = - \sum_{m,n} (t_x^+ c_{m+1,n}^\dagger c_{m,n} + t_x^- c_{m,n}^\dagger c_{m+1,n} + t_e^{i2\pi m\phi} c_{m,n+1}^\dagger c_{m,n} + t_e^{-i2\pi m\phi} c_{m,n}^\dagger c_{m,n+1}), \quad (1)$$

where $c_{m,n}^\dagger$ ($c_{m,n}$) are the creation (annihilation) operator on the site (m, n) , $t_x^\pm = t \pm \delta_x$ describe the

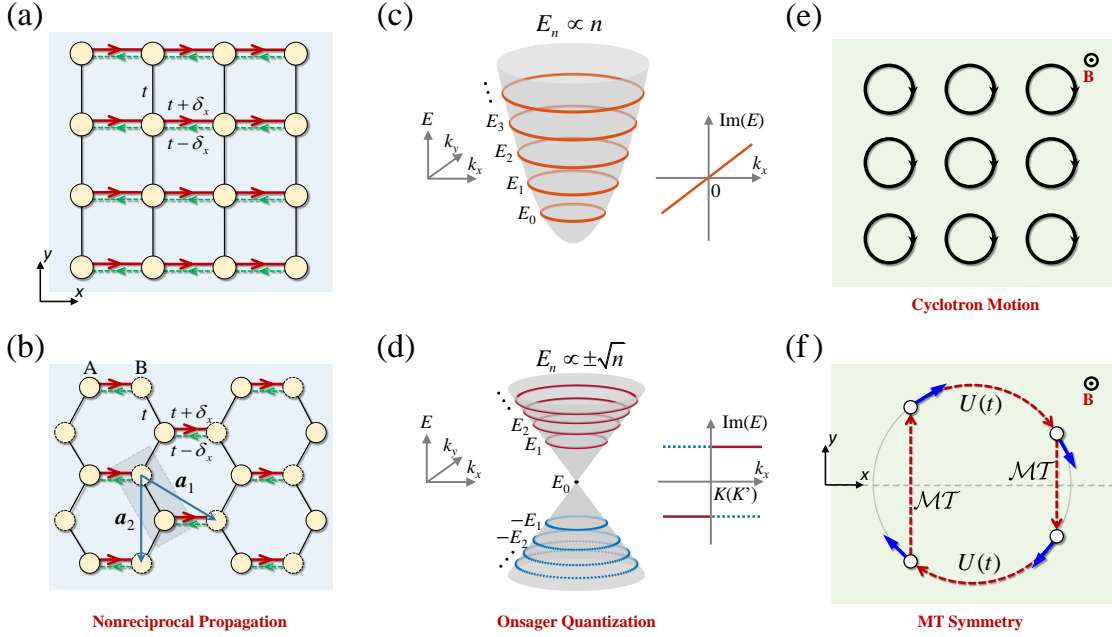


FIG. 1: Schematic illustration of (a) nonreciprocal Harper-Hofstadter model and (b) nonreciprocal honeycomb lattice model with unequal hopping strengths $t \pm \delta_x$ in the x -direction and equal hopping t in others. The gray dashed box in (b) denotes the unit cell composed of two sites A, B and $\mathbf{a}_{1,2}$ are the unit vectors. (c) Low-energy parabolic dispersion with the linear imaginary part corresponding to the square lattice model in (a). (d) Dirac cone dispersion and its imaginary part corresponding to the honeycomb lattice in (b). The signs of the imaginary part of the energy coincide with those of the velocity. The contours in (c) and (d) are the closed orbits that satisfy the Onsager-Lifshitz quantization rule. (e) Semiclassical cyclotron motion of charged particles in a magnetic field. (f) Semiclassical picture of the \mathcal{MT} symmetry, in which the successive actions of the \mathcal{MT} operation ($y \rightarrow -y, v_x \rightarrow -v_x$) and the time evolution $U(t)$ leave the state unchanged.

nonreciprocal hopping in the x -direction with δ_x the strength of nonreciprocity. The phase factor $\phi = \Phi/\Phi_0$ is defined by the magnetic flux $\Phi = Ba^2$ through a lattice cell (lattice constant a) divided by the flux quantum $\Phi_0 = h/q$ with q the charge of the particle. Here, the Landau gauge $\mathbf{A} = (0, Bx)$ has been adopted. In the rest of this Letter, we set $h = q = a = 1$ in all numerical calculations for simplicity and denote the OBC and PBC in the α -direction ($\alpha = x, y$) as α -OBC and α -PBC for brevity.

For $B = 0$, the energy spectrum under the x, y -PBC is $E(\mathbf{k}) = -2t(\cos k_x + \cos k_y) + 2i\delta_x \sin k_x$ with $\mathbf{k} = (k_x, k_y)$ the wave vector. The low-energy expansion at the band bottom yields the parabolic dispersion plus an imaginary part as $\varepsilon(\mathbf{k}) = t(k_x^2 + k_y^2) + 2i\delta_x k_x$; see Fig. 1(c), which resembles a non-Hermitian normal particle. The odd function with $\text{Im}[E(k_x)] = -\text{Im}[E(-k_x)]$ induces a point gap topology for each transverse k_y -mode, which results in the nonreciprocal propagation of the wave packet in the x -direction [53, 54]. Accordingly, the system exhibits NHSE in the x -direction under the x -OBC [37–39], which can be read from the right eigenfunctions of Eq. (1) under the x, y -OBC as $\psi^R(x, y) = \psi_{m,n} = (t_x^+/t_x^-)^{m/2} \sin(mk_x) \sin(nk_y)$. A positive δ_x results in

an envelope function $(t_x^+/t_x^-)^{m/2}$ on top of the standing waves so that all the wave functions are localized at the right boundary, namely NHSE. Due to its incompatibility, a small magnetic field is sufficient to drive the skin modes to penetrate deeply into the bulk, showing a considerable suppression of the NHSE [64, 65]. Physically, it stems from the shrinkage of the point gap for each k_y channel, i.e., a reduction of the nonreciprocity [64].

Semiclassical Onsager-Lifshitz quantization.—It is of particular interest to investigate the semiclassical quantization of magnetic cyclotron orbits subject to nonreciprocal propagation. Intuitively, nonreciprocity tends to break those closed orbits [cf. Fig. 1(e)] and thus the quantization condition. To study the wave packet dynamics inside the bulk and get rid of the boundary effects, we adopt the x, y -PBC. The Hamiltonian (1) can be written in momentum space and diagonalized directly, with the energy spectra for $\delta_x = 0$ and $\delta_x > 0$ shown in Figs. 2(a) and 2(b), respectively.

For $\delta_x = 0$, Fig. 2(a) presents the familiar butterfly diagram. The Landau fan structure near the band edges for small B indicates the high degeneracy of Landau levels with vanishing band width, which stems from localized cyclotron motion. A finite nonreciprocal hopping δ_x

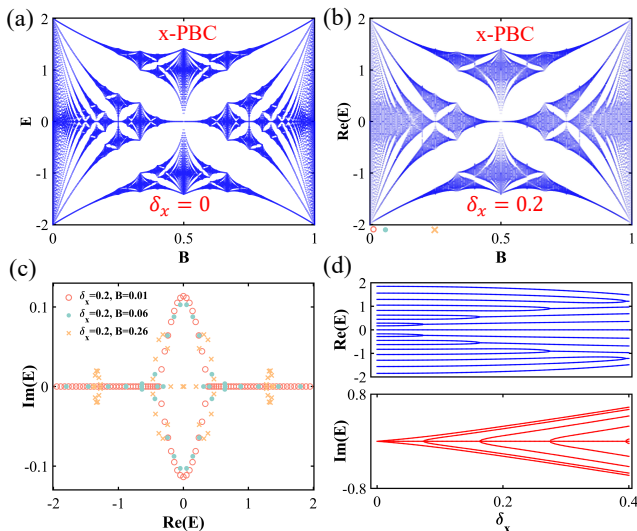


FIG. 2: Energy spectra under the x, y -PBC calculated in the momentum space for (a) $\delta_x = 0$ and (b) $\delta_x = 0.2$. (c) Complex energy spectra for different B marked in (b). (d) Complex energy spectra as a function of δ_x with $B = 0.05$. In all figures, $t = 0.5$.

leads to visible modifications in the energy spectra with complex energy spectra showing up at the band center; see Figs. 2(b) and (c). As a result, the self-similar fractal patterns merge into continuous pieces along with multiple gap closings. Notably, as δ_x increases, the energy levels coalesce in pairs and create multiple exceptional points; see Fig. 2(d). Given the high degeneracy of the magnetic spectra, a large number of exceptional points can be implemented in such systems.

Remarkably, one can find that the Landau levels near the band top and bottom remain unchanged despite the nonreciprocity by comparing Figs. 2(a) and 2(b). Moreover, these low-energy Landau levels remain real [see Fig. 2(c)], which indicates that the magnetic field prevents the system from a real-to-complex spectral transition in the long-wavelength limit. It can be shown that the quantized energy levels exhibit the scaling $E_n \propto nB$ [64], which reduces to the behavior of free particles with a quadratic dispersion [cf. Fig. 1(c)]. Such observations indicate that the Onsager-Lifshitz quantization rule [66, 67] remains valid even in the presence of nonreciprocal propagation.

We prove this assertion based on the semiclassical equation of motion. In the long-wavelength limit, the effective Hamiltonian in a magnetic field can be written as $\varepsilon(\mathbf{p} - q\mathbf{A}) = t(\mathbf{p} - q\mathbf{A})^2 + 2i\delta_x k_x$ through Peierls substitution $\hbar\mathbf{k} \rightarrow \mathbf{p} - q\mathbf{A}$ with \mathbf{p} the canonical momentum. By solving the canonical equation $\dot{\mathbf{p}} = -\nabla_{\mathbf{r}}\varepsilon$, $\dot{\mathbf{r}} = \nabla_{\mathbf{p}}\varepsilon$, we obtain the time(τ)-dependent coordinate functions

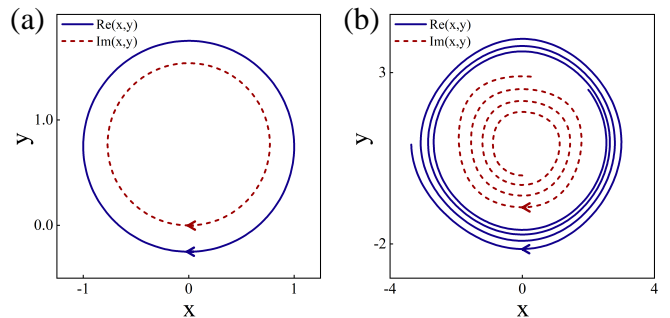


FIG. 3: Projections of the semiclassical trajectories in the real and imaginary x - y planes. (a) Closed orbits in the long-wavelength limit with $x(0) = 1$, $y(0) = 0.75$, $p_x(0) = 0$, $p_y(0) = 0$ and (b) open trajectories beyond this limit with $x(0) = 2$, $y(0) = 2.5$, $p_x(0) = 0.4$, $p_y(0) = 0$. Other parameters are $B = 0.26$, $\delta_x = 0.1$.

as [64]

$$\begin{aligned} x(\tau) &= A_1 e^{i\omega\tau} + A_2 e^{-i\omega\tau} + x_0, \\ y(\tau) &= i(A_1 e^{i\omega\tau} - A_2 e^{-i\omega\tau}) + y_0, \end{aligned} \quad (2)$$

with the parameters $A_{1,2}, x_0, y_0$ determined by the initial conditions and $\omega = 2Btq/\hbar^2$ the cyclotron frequency. The solutions clearly show that the semiclassical trajectories of the wave packet always form closed orbits despite the nonreciprocity; see Fig. 3(a). However, different from the Hermitian case, the closed orbits generally reside in 4D complex x - y space [2].

Although closed orbits are formed in higher-dimensional coordinate space, the single-valuedness of the wave function for the periodic motion still imposes the quantization condition, which is the non-Hermitian Onsager-Lifshitz quantization rule [66, 67]:

$$\oint \mathbf{p} \cdot d\mathbf{r} = (n + \frac{1}{2})\hbar. \quad (3)$$

Substituting the solutions $\mathbf{p}(\tau), \mathbf{r}(\tau)$ into the quantization condition results in exactly the Landau levels $\varepsilon_n = (n + 1/2)\hbar\omega + \delta_x^2/t$ of a normal particle apart from a small shift δ_x^2/t [64], consistent with the numerical results in Fig. 2(b). Therefore, we conclude that the semiclassical quantization is robust against the nonreciprocity and thus can protect the energy from being complex. Meanwhile, as $E(\mathbf{k})$ deviates from the long-wavelength limit, the coordinate functions can be solved numerically, which exhibit unclosed trajectories in the complex x - y space; see Fig. 3(b). As a result, the energy spectra become complex due to the nonreciprocal hopping as those in Figs. 2(b) and (c).

MT phase transition.—The properties of the whole energy spectra strongly depend on the boundary conditions in the x -direction. The magnetic spectra are entirely real for the x -OBC [64] and partially complex for the x -PBC.

We will show that a real-to-complex transition of the entire spectra can be implemented, which is associated with the spontaneous breaking of the inherent \mathcal{MT} symmetry of the systems.

The Hamiltonian (1) possesses the combined \mathcal{MT} symmetry as

$$\mathcal{MTH}(\mathcal{MT})^{-1} = H, \quad (4)$$

with the operators of mirror reflection (\mathcal{M}) about the x -axis and time reversal (\mathcal{T}) defined by

$$\mathcal{M}c_{m,n}\mathcal{M}^{-1} = c_{m,-n}, \mathcal{T}c_{m,n}\mathcal{T}^{-1} = c_{m,n}, \mathcal{T}i\mathcal{T}^{-1} = -i. \quad (5)$$

The \mathcal{MT} symmetry can be understood by the semi-classical picture as illustrated in Fig. 1(f). A quantum state under successive actions of the \mathcal{MT} operation and the time evolution $U(t)$ remains the same, i.e., $U(t)\mathcal{MT}U(t)\mathcal{MT} = 1$. The constraint by the \mathcal{MT} symmetry can be rewritten in another standard form as $\mathcal{M}\mathcal{O}H^\dagger(\mathcal{M}\mathcal{O})^{-1} = H$, with \mathcal{O} the transpose operation, and then H is said to be $\mathcal{M}\mathcal{O}$ -pseudo-Hermitian [3]. As a result, the energy spectra can be either entirely real or composed of complex conjugate pairs. For a specific state, the real (complex) nature of the energy corresponds to its wave function with (without) the \mathcal{MT} symmetry [68].

The \mathcal{MT} -symmetry breaking for the i th right eigenstate ψ_i^R can be measured by the Hilbert-Schmidt quantum distance d_{HS}^i [69], which is given by

$$d_{\text{HS}}^i = \sqrt{1 - |\langle \mathcal{MT} \rangle_i|^2}, \quad \langle \mathcal{MT} \rangle_i = \langle \psi_i^R | \mathcal{MT} | \psi_i^R \rangle. \quad (6)$$

It characterizes the quantum mechanical distance between the wave functions before and after the \mathcal{MT} operation. For the state that satisfies the \mathcal{MT} symmetry, the \mathcal{MT} operation yields only an overall phase factor, i.e., $\mathcal{MT}|\psi_i^R\rangle = e^{i\theta}|\psi_i^R\rangle$, so that $d_{\text{HS}}^i = 0$. In contrast, if the state breaks the \mathcal{MT} symmetry, one has $0 < d_{\text{HS}}^i \leq 1$.

It is convenient to introduce an *order parameter* to quantify the spontaneous symmetry breaking in non-Hermitian phase transitions. An insightful choice of the order parameter can be the average quantum distance of all \mathcal{N} eigenstates defined as

$$d_{\text{HS}} = \frac{1}{\mathcal{N}} \sum_i^{\mathcal{N}} d_{\text{HS}}^i. \quad (7)$$

The \mathcal{MT} -symmetric and \mathcal{MT} -broken phases correspond to $d_{\text{HS}} = 0$ and $d_{\text{HS}} > 0$, respectively, resembling the spontaneous symmetry breaking in continuous phase transitions. Importantly, in addition to being a criterion of the \mathcal{MT} transition, the magnitude of d_{HS} can tell to what extent the \mathcal{MT} symmetry is broken.

A tunable boundary condition [26, 70] that can drive a continuous \mathcal{MT} transition is defined by the boundary hopping $-\gamma_B(t_x^+ c_{1,n}^\dagger c_{M,n} + t_x^- c_{M,n}^\dagger c_{1,n})$. The

parameter $\gamma_B \in [0, 1]$ and its two limits $\gamma_B = 0$ and $\gamma_B = 1$ correspond to the x -OBC and x -PBC, respectively. We perform Fourier transformation to the bulk Hamiltonian in the y -direction and rewrite it as $\tilde{H} = -\sum_{m,k_y} [t_x^+ c_{m+1,k_y}^\dagger c_{m,k_y} + t_x^- c_{m,k_y}^\dagger c_{m+1,k_y} + 2t \cos(k_y + 2\pi m\phi) c_{m,k_y}^\dagger c_{m,k_y}]$. Its eigenstates $\psi_i^R(m, k_y)$ are labeled by i and k_y . In this representation, it can be proved that the \mathcal{MT} operator acts on the wave function as $\mathcal{MT}\psi_i^R(m, k_y) = \psi_i^{R*}(m, k_y)$. The order parameter d_{HS} as a function of γ_B and δ_x can be calculated by Eq. (7), in which the average is taken over all states labeled by i and k_y .

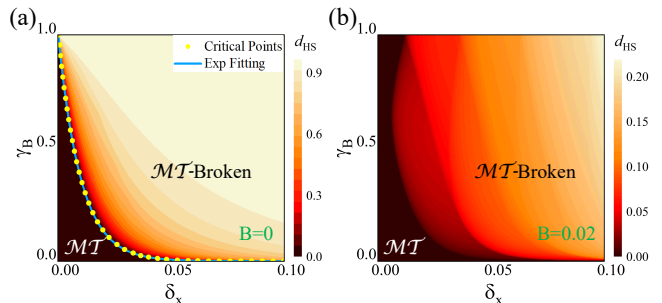


FIG. 4: Order parameter d_{HS} as a function of δ_x and γ_B for the nonreciprocal square lattice with (a) $B = 0$ and (b) $B = 0.02$. Critical points in (a) mark the real-to-complex spectral transition and the phase boundary defined by the d_{HS} contours is fitted by exponential functions. Other parameters are $M = 50$, $t = 0.5$.

Numerical results of d_{HS} for zero and finite B are shown in Fig. 4. One can see that there is a clear phase boundary formed between the \mathcal{MT} -symmetric ($d_{\text{HS}} = 0$) and \mathcal{MT} -broken ($d_{\text{HS}} > 0$) regions. Such a phase boundary can also be obtained by the critical points of the real-to-complex spectral transition as usually done in the literature, and the phase boundaries obtained by the two methods show good coincidence; see Fig. 4(a). This is assured by the theorem associated with the \mathcal{MT} antiunitary symmetry [68]. Interestingly, the critical phase boundary in Fig. 4(a) turns out to be exponential functions, which can be strictly proved [64].

Without a magnetic field, the system is in the \mathcal{MT} -symmetric and \mathcal{MT} -broken phases under the x -OBC ($\gamma_B = 0$) and x -PBC ($\gamma_B = 1$), respectively; see Fig. 4(a). By tuning the boundary parameter γ_B , a continuous \mathcal{MT} transition connecting two limiting cases can be implemented. However, varying with δ_x , there is no phase transition happening in either the x -OBC or the x -PBC. Remarkably, a finite magnetic field can effectively suppress the \mathcal{MT} -symmetry breaking; see Fig. 4(b), which is reflected in two aspects. First, the \mathcal{MT} -symmetric region with large γ_B expands with B increased. Second, the order parameter d_{HS} diminishes

in the \mathcal{MT} -broken region so that the symmetry breaking becomes weaker, which is consistent with the magnetic field induced real Landau levels. These results reflect the incompatible nature between the nonreciprocity and the magnetic field. Such magnetic suppression on the \mathcal{MT} -symmetry breaking indicates that a \mathcal{MT} transition can be driven by either δ_x or B for a finite system [64].

In the discussion above, the hopping strength t_x is chosen to be real. By adding a small imaginary part $i\eta$ to the hopping terms as $\tilde{t}_x^\pm = t + i\eta \pm \delta_x$, the \mathcal{MT} symmetry of the Hamiltonian in Eq. (4) is destroyed. As a result, the energy spectra become entirely complex without any \mathcal{MT} transition. This further proves that the \mathcal{MT} dictates the spectral transition; see Supplemental Material for details [64].

Results for nonreciprocal honeycomb lattice.- The interplay between the nonreciprocity and a magnetic field possesses a general picture so that the physical results are expected to be universal. To verify this, we perform parallel investigations on the nonreciprocal honeycomb lattice [64]; see Fig. 1(b), whose low-energy physics corresponds to the non-Hermitian massless Dirac particle as sketched in Fig. 1(d). We show that the main results obtained in the main text hold true for the nonreciprocal honeycomb lattice as well [64]. Specifically, the quantization rule persists against nonreciprocity in the long-wavelength limit, which gives rise to the familiar Landau levels $\varepsilon_n^D \propto \pm\sqrt{n}B$ for massless Dirac particles [cf. Figs. 1(d)]. The closed cyclotron orbits formed in the complex space are the physical origin of the semiclassical quantization. The \mathcal{MT} phase transition can also be implemented on the honeycomb lattice, which exhibits similar phase diagrams and magnetic suppression on the \mathcal{MT} -symmetry breaking; see the Supplemental Material for details [64].

Acknowledgments.- We thank Zhong Wang, Chen Fang, Zhesen Yang, Rui Wang, L. B. Shao, J. L. Lado and Oded Zilberberg for helpful discussions. This work was supported by the National Natural Science Foundation of China under Grant No. 12074172 (W.C.), No. 12222406 (W.C.) and No. 12174182 (D.Y.X.), Fundamental Research Funds for the Central Universities (W.C.), the startup grant at Nanjing University (W.C.), the State Key Program for Basic Researches of China under Grants No. 2021YFA1400403 (D.Y.X.) and the Excellent Programme at Nanjing University.

* Corresponding author: pchenweis@gmail.com

[1] C. M. Bender and S. Boettcher, Phys. Rev. Lett. **80**, 5243 (1998).
 [2] C. M. Bender, Reports on Progress in Physics **70**, 947 (2007).
 [3] Y. Ashida, Z. Gong, and M. Ueda, Advances in Physics **69**, 249 (2020).

[4] L. Feng, R. El-Ganainy, and L. Ge, Nature Photonics **11**, 752 (2017).
 [5] T. Ozawa, H. M. Price, A. Amo, N. Goldman, M. Hafezi, L. Lu, M. C. Rechtsman, D. Schuster, J. Simon, O. Zilberberg, and I. Carusotto, Rev. Mod. Phys. **91**, 015006 (2019).
 [6] W. Chen, Ş. K. Özdemir, G. Zhao, J. Wiersig, and L. Yang, Nature **548**, 192 (2017).
 [7] R. El-Ganainy, K. G. Makris, M. Khajavikhan, Z. H. Musslimani, S. Rotter, and D. N. Christodoulides, Nature Physics **14**, 11 (2018).
 [8] Ş. K. Özdemir, S. Rotter, F. Nori, and L. Yang, Nature materials **18**, 783 (2019).
 [9] M.-A. Miri and A. Alu, Science **363**, 42 (2019).
 [10] I. Rotter, Reports on Progress in Physics **54**, 635 (1991).
 [11] I. Rotter, Journal of Physics A: Mathematical and Theoretical **42**, 153001 (2009).
 [12] S. Malzard, C. Poli, and H. Schomerus, Phys. Rev. Lett. **115**, 200402 (2015).
 [13] S. Diehl, A. Micheli, A. Kantian, B. Kraus, H. Büchler, and P. Zoller, Nature Physics **4**, 878 (2008).
 [14] V. Kozii and L. Fu, “Non-hermitian topological theory of finite-lifetime quasiparticles: Prediction of bulk fermi arc due to exceptional point,” (2017), arXiv:1708.05841 [cond-mat.mes-hall].
 [15] H. Shen and L. Fu, Phys. Rev. Lett. **121**, 026403 (2018).
 [16] M. Papaj, H. Isobe, and L. Fu, Phys. Rev. B **99**, 201107 (2019).
 [17] T. Yoshida, R. Peters, and N. Kawakami, Phys. Rev. B **98**, 035141 (2018).
 [18] J. Schindler, A. Li, M. C. Zheng, F. M. Ellis, and T. Kottos, Phys. Rev. A **84**, 040101 (2011).
 [19] C. H. Lee, S. Imhof, C. Berger, F. Bayer, J. Brehm, L. W. Molenkamp, T. Kiessling, and R. Thomale, Communications Physics **1**, 1 (2018).
 [20] T. Kotwal, F. Moseley, A. Stegmaier, S. Imhof, H. Brand, T. Kießling, R. Thomale, H. Ronellenfitsch, and J. Dunkel, Proceedings of the National Academy of Sciences **118** (2021).
 [21] J. Ningyuan, C. Owens, A. Sommer, D. Schuster, and J. Simon, Phys. Rev. X **5**, 021031 (2015).
 [22] S. Imhof, C. Berger, F. Bayer, J. Brehm, L. W. Molenkamp, T. Kiessling, F. Schindler, C. H. Lee, M. Greiter, T. Neupert, *et al.*, Nature Physics **14**, 925 (2018).
 [23] H. Shen, B. Zhen, and L. Fu, Phys. Rev. Lett. **120**, 146402 (2018).
 [24] E. J. Bergholtz, J. C. Budich, and F. K. Kunst, Rev. Mod. Phys. **93**, 015005 (2021).
 [25] T. E. Lee, Phys. Rev. Lett. **116**, 133903 (2016).
 [26] Y. Xiong, Journal of Physics Communications **2**, 035043 (2018).
 [27] Z. Gong, Y. Ashida, K. Kawabata, K. Takasan, S. Higashikawa, and M. Ueda, Phys. Rev. X **8**, 031079 (2018).
 [28] K. Kawabata, S. Higashikawa, Z. Gong, Y. Ashida, and M. Ueda, Nature communications **10**, 1 (2019).
 [29] Y. Xu, S.-T. Wang, and L.-M. Duan, Phys. Rev. Lett. **118**, 045701 (2017).
 [30] J. Carlström, M. Stålhammar, J. C. Budich, and E. J. Bergholtz, Phys. Rev. B **99**, 161115 (2019).
 [31] B. Peng, Ş. K. Özdemir, F. Lei, F. Monifi, M. Gianfreda, G. L. Long, S. Fan, F. Nori, C. M. Bender, and L. Yang, Nature Physics **10**, 394 (2014).

- [32] P. St-Jean, V. Goblot, E. Galopin, A. Lemaître, T. Ozawa, L. Le Gratiet, I. Sagnes, J. Bloch, and A. Amo, *Nature Photonics* **11**, 651 (2017).
- [33] M. Parto, S. Wittek, H. Hodaie, G. Harari, M. A. Bandres, J. Ren, M. C. Rechtsman, M. Segev, D. N. Christodoulides, and M. Khajavikhan, *Phys. Rev. Lett.* **120**, 113901 (2018).
- [34] S. Yao and Z. Wang, *Phys. Rev. Lett.* **121**, 086803 (2018).
- [35] F. K. Kunst, E. Edvardsson, J. C. Budich, and E. J. Bergholtz, *Phys. Rev. Lett.* **121**, 026808 (2018).
- [36] K. Yokomizo and S. Murakami, *Phys. Rev. Lett.* **123**, 066404 (2019).
- [37] D. S. Borgnia, A. J. Kruchkov, and R.-J. Slager, *Phys. Rev. Lett.* **124**, 056802 (2020).
- [38] K. Zhang, Z. Yang, and C. Fang, *Phys. Rev. Lett.* **125**, 126402 (2020).
- [39] N. Okuma, K. Kawabata, K. Shiozaki, and M. Sato, *Phys. Rev. Lett.* **124**, 086801 (2020).
- [40] Z. Yang, K. Zhang, C. Fang, and J. Hu, *Phys. Rev. Lett.* **125**, 226402 (2020).
- [41] L. Li, C. H. Lee, S. Mu, and J. Gong, *Nature communications* **11**, 1 (2020).
- [42] T. Helbig, T. Hofmann, S. Imhof, M. Abdelghany, T. Kiessling, L. Molenkamp, C. Lee, A. Szameit, M. Greiter, and R. Thomale, *Nature Physics* **16**, 747 (2020).
- [43] L. Xiao, T. Deng, K. Wang, G. Zhu, Z. Wang, W. Yi, and P. Xue, *Nature Physics* **16**, 761 (2020).
- [44] S. Weidemann, M. Kremer, T. Helbig, T. Hofmann, A. Stegmaier, M. Greiter, R. Thomale, and A. Szameit, *Science* **368**, 311 (2020).
- [45] A. Ghatak, M. Brandenbourger, J. van Wezel, and C. Coulais, *Proceedings of the National Academy of Sciences* **117**, 29561 (2020).
- [46] L. S. Palacios, S. Tchoumakov, M. Guix, I. Pagonabarraga, S. Sánchez, and A. G. Grushin, *Nature Communications* **12**, 1 (2021).
- [47] X. Zhang, Y. Tian, J.-H. Jiang, M.-H. Lu, and Y.-F. Chen, *Nature communications* **12**, 1 (2021).
- [48] Q. Liang, D. Xie, Z. Dong, H. Li, H. Li, B. Gadway, W. Yi, and B. Yan, *arXiv preprint arXiv:2201.09478* (2022).
- [49] S. Longhi, *Optics letters* **44**, 5804 (2019).
- [50] S. Longhi, *Phys. Rev. Research* **1**, 023013 (2019).
- [51] L. Xiao, T. Deng, K. Wang, Z. Wang, W. Yi, and P. Xue, *Phys. Rev. Lett.* **126**, 230402 (2021).
- [52] F. Song, H.-Y. Wang, and Z. Wang, *arXiv preprint arXiv:2102.02230* (2021).
- [53] Y. Yi and Z. Yang, *Phys. Rev. Lett.* **125**, 186802 (2020).
- [54] W.-T. Xue, M.-R. Li, Y.-M. Hu, F. Song, and Z. Wang, *Phys. Rev. B* **103**, L241408 (2021).
- [55] N. Hatano and D. R. Nelson, *Phys. Rev. Lett.* **77**, 570 (1996).
- [56] H. Jiang, L.-J. Lang, C. Yang, S.-L. Zhu, and S. Chen, *Phys. Rev. B* **100**, 054301 (2019).
- [57] Y. Liu, Y. Wang, Z. Zheng, and S. Chen, *Phys. Rev. B* **103**, 134208 (2021).
- [58] J. R. Abo-Shaer, C. Raman, J. M. Vogels, and W. Ketterle, *Science* **292**, 476 (2001).
- [59] Y.-J. Lin, R. L. Compton, K. Jiménez-García, J. V. Porto, and I. B. Spielman, *Nature* **462**, 628 (2009).
- [60] X.-X. Zhang and M. Franz, *Phys. Rev. Lett.* **124**, 046401 (2020).
- [61] Z. Lin, L. Ding, S. Ke, and X. Li, *Optics Letters* **46**, 3512 (2021).
- [62] P. G. Harper, *Proceedings of the Physical Society. Section A* **68**, 874 (1955).
- [63] D. R. Hofstadter, *Phys. Rev. B* **14**, 2239 (1976).
- [64] See Supplemental Material for the suppression of the NHSE effect, scaling of the low-energy Landau levels, derivation of the semiclassical orbits and real Landau levels determined by the quantization conditions, magnetic spectra under the x -OBC, the proof of the exponential phase boundary, the size effect of the \mathcal{MT} phase transition, \mathcal{MT} -breaking of the Hamiltonian by non-Hermitian complex hopping and physical results for the nonreciprocal honeycomb lattice, which includes Ref. [70].
- [65] M. Lu, X.-X. Zhang, and M. Franz, *Phys. Rev. Lett.* **127**, 256402 (2021).
- [66] L. Onsager, *The London, Edinburgh, and Dublin Philosophical Magazine and Journal of Science* **43**, 1006 (1952).
- [67] I. Lifshitz and A. Kosevich, *Dokl. Akad. Nauk SSSR* **96**, 963 (1954).
- [68] E. P. Wigner, in *The Collected Works of Eugene Paul Wigner* (Springer, 1993) pp. 551–555.
- [69] A. Shapere and F. Wilczek, *Geometric phases in physics*, Vol. 5 (World scientific, 1989).
- [70] C.-X. Guo, C.-H. Liu, X.-M. Zhao, Y. Liu, and S. Chen, *Phys. Rev. Lett.* **127**, 116801 (2021).

Supplemental Material for ‘‘Cyclotron quantization and mirror-time transition on nonreciprocal lattices’’

I. SUPPRESSION OF NHSE BY A MAGNETIC FIELD

In this section, we show that a magnetic field can effectively suppress the NHSE. Its physical reason is the shrinkage of the point gap for each k_y channel. We present first the results for the nonreciprocal square lattice and then those for the nonreciprocal honeycomb lattice.

A. Nonreciprocal square lattice

Given that there is no nonreciprocity in the y -direction, meaning that the boundary condition in this direction is unimportant, we set the y -PBC for simplicity. The Hamiltonian can then be Fourier transformed into $\tilde{H} = -\sum_{m,k_y} [t_x^+ c_{m+1,k_y}^\dagger c_{m,k_y} + t_x^- c_{m,k_y}^\dagger c_{m+1,k_y} + 2t \cos(k_y + 2\pi m\phi) c_{m,k_y}^\dagger c_{m,k_y}]$. Taking the x -OBC, we plot in Fig. S.1(a) the spatial distribution function $W(x, k_y) = \sum_i |\psi_i^R(m, k_y)|^2 / M$ defined by all the right eigenstates $\psi_i^R(m, k_y)$ (labeled by i) of \tilde{H} for a given k_y . One can see that a small B is sufficient to drive the skin modes to penetrate deeply into the bulk, showing a considerable suppression of the NHSE. This result generally holds for all transverse wave vectors k_y .

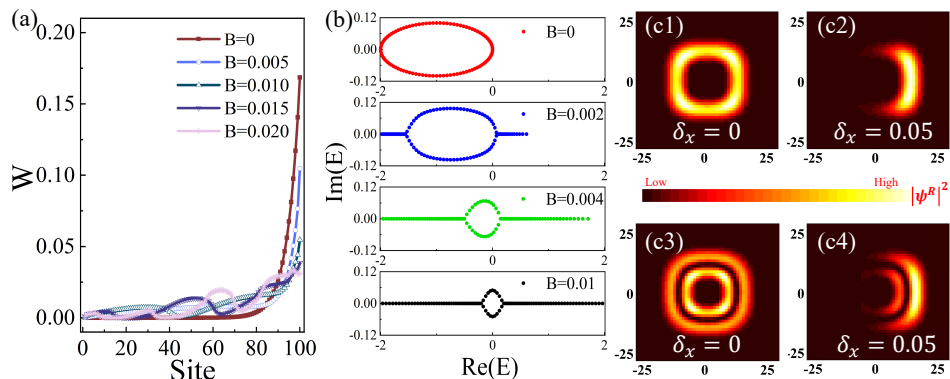


FIG. S.1: (a) Spatial distribution functions $W(x, k_y)$ under the x -OBC and y -PBC. (b) Complex energy spectra under the x, y -PBC for different B with $\delta_x = 0.05$, $M = 100$ and $k_y = 0$. (c1-c4) Modulation of the wave functions by the nonreciprocal hopping δ_x . (c1,c2) The 8th and (c3,c4) 58th eigenstates numbered by ascending $\text{Re}(E)$ are randomly chosen and other parameters are $B = 0.02$ and $M = N = 50$. In all figures, $t = 0.5$.

The above results can be understood by the following pictures. At $B = 0$, the energy spectra $E_{k_y}(k_x)$ for a given k_y forms a closed loop with a point gap topology in its complex plane under the x -PBC; see Fig. S.1(b), indicating the presence of the NHSE under the x -OBC. For a finite B , real energy spectra develop from the band edges to the center with B increased, accompanied by a shrinkage of the complex loop; see Fig. S.1(b). According to the correspondence between the spectra under the x -PBC and the NHSE under the x -OBC, this means that a magnetic field tends to suppress the NHSE. One can also analyze the results from the real-space perspective under the x, y -OBC and start with the opposite limit of $\delta_x = 0$. With increasing δ_x from zero, the wave functions under the magnetic field are modulated by the exponential envelope function introduced by the NHSE; see Figs. S.1(c1-c4). Then the results in Fig. S.1(a) can be understood as the superposition of all the broken loops in real space.

B. Nonreciprocal honeycomb lattice

Next, we investigate the nonreciprocal honeycomb lattice in Fig. 1(b) of the main text. With the same Landau gauge $\mathbf{A} = (0, Bx)$ adopted and the zigzag edges oriented along the y -direction, the Hamiltonian for the nonreciprocal

honeycomb lattice reads

$$\begin{aligned}
 H' = & \sum_{mn} (t_x^+ b_{m+1,n}^\dagger a_{m,n} + t_x^- a_{m,n}^\dagger b_{m+1,n}) \\
 & + t \sum_{mn} (e^{i2\pi\phi' m} b_{m,n}^\dagger a_{m,n} + e^{-i2\pi\phi' m} b_{m,n+1}^\dagger a_{m,n} + \text{H.c.}),
 \end{aligned}
 \tag{S.1}$$

where $a_{m,n}^\dagger, b_{m,n}^\dagger$ ($a_{m,n}, b_{m,n}$) are the creation (annihilation) operators for the A, B sublattices, respectively, and $\mathbf{R}_{(m,n)} = m\mathbf{a}_1 + n\mathbf{a}_2$ is the location of the lattice sites with $(\mathbf{a}_1, \mathbf{a}_2)$ the unit vectors shown in Fig. 1(b) of the main text. The phase factor is defined by $\phi' = \Phi'/(2\Phi_0)$ with $\Phi' = 3\sqrt{3}Ba'^2/2$ the flux through a unit cell and a' the bond length that is set to $a' = 1$ henceforth.

Similar to the square lattice, we take the y -PBC and rewrite the Hamiltonian into $\tilde{H}' = \sum_{m,k_y} [\Delta a_{m,k_y}^\dagger b_{m,k_y} + \Delta^* b_{m,k_y}^\dagger a_{m,k_y} + t_x^+ b_{m+1,k_y}^\dagger a_{m,k_y} + t_x^- a_{m,k_y}^\dagger b_{m+1,k_y}]$ with $\Delta = 2t \cos[\sqrt{3}k_y/2 + \pi\phi(m - 5/6)]$. The spatial distribution function is calculated by $W'(x, k_y) = \sum_i (|\psi_{a,i}^R(m, k_y)|^2 + |\psi_{b,i}^R(m, k_y)|^2)/(2M)$ with $\psi_{a,i}^R(m, k_y)$ and $\psi_{b,i}^R(m, k_y)$ the components on the A and B sublattices, respectively. The spatial distribution $W'(x, k_y)$ is plotted in Fig. S.2(a). Similar to the results of the square lattice, the skin modes are strongly suppressed by just a small B . It is closely related to the shrinkage of two complex loops of the energy spectra under the x -PBC (for an arbitrary k_y); see Fig. S.2(b). The conclusions agree with those of the square lattice in Sec.I.A.

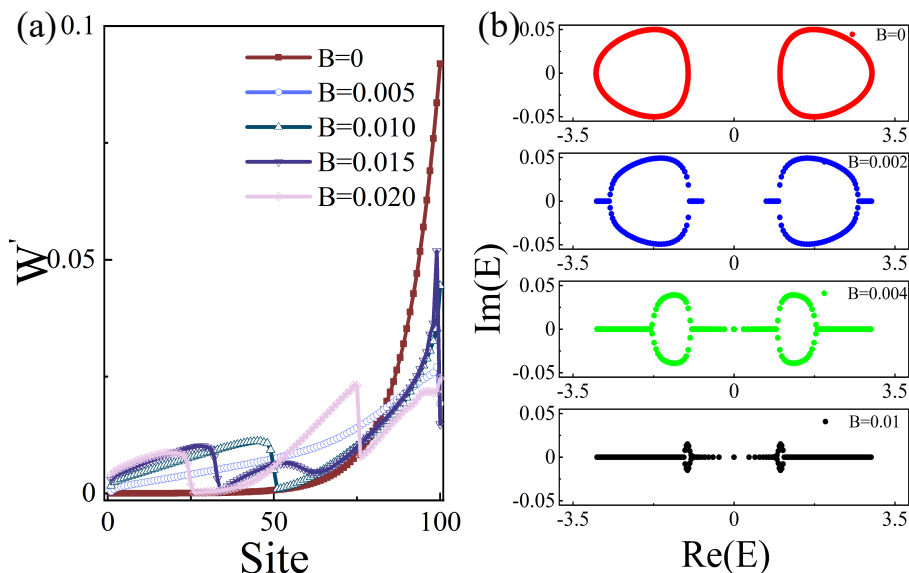


FIG. S.2: (a) The spatial distribution functions $W'(x, k_y)$ under the x -OBC and y -PBC and (b) the complex energy spectra under the x -PBC and y -PBC for different B with $\delta_x = 0.05$, $t = 1$, $M = 200$ and $k_y = 0$.

II. SCALING OF LOW-ENERGY LANDAU LEVELS

Fig. S.3 shows the energy spectra for different δ_x under the x -PBC. One can see that the spectra undergo a visible modification as δ_x increases. Interestingly, the Landau fan structures with real energy values persist in the long-wavelength limit. Figs. S.3(e-h) show that the Landau levels exhibit the scaling $E_n \propto nB$, which resembles the normal particle behavior. Such numerical results can be well explained by the semiclassical quantization introduced in the next section.

III. SEMICLASSICAL ORBITS AND QUANTIZATION CONDITIONS

In this section, we derive the time-dependent coordinate functions and the trajectories of the wave packet under a magnetic field based on the semiclassical equation of motion for both the nonreciprocal square and honeycomb

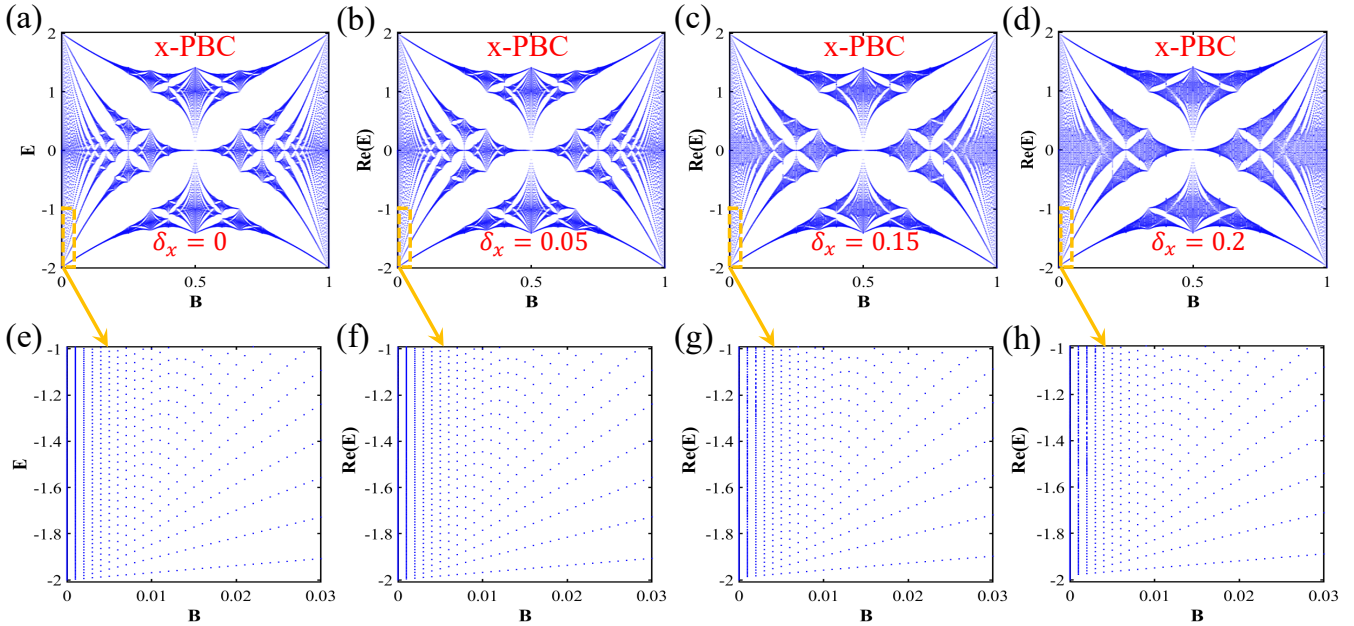


FIG. S.3: (a-d) Energy spectra under the x -PBC and y -PBC with $\delta_x = 0, 0.05, 0.15, 0.2$ and $t = 0.5$. (e-h) Zoom of the Landau fan structures corresponding to (a-d).

lattices. We show that, in the long-wavelength limit, the semiclassical orbits are always closed loops, which give rise to real Landau levels. Beyond the long-wavelength limit, the orbits become open and the energies are complex.

A. Nonreciprocal square lattice

Without a magnetic field, the eigenenergy of Hamiltonian (1) in the main text is

$$E(\mathbf{k}) = -2t(\cos k_x + \cos k_y) - 2i\delta_x \sin k_x \quad (\text{S.2})$$

The Hamiltonian under a magnetic field can be obtained through the Peierls substitution ($\hbar\mathbf{k} \rightarrow \mathbf{p} - q\mathbf{A}$) as

$$h = -2[t \cos p_x + t \cos(p_y - Bx) + i\delta_x \sin p_x], \quad (\text{S.3})$$

where $\mathbf{A} = (0, Bx)$ and $\hbar = q = a = 1$ have been adopted. The Hamilton's canonical equations read

$$\begin{aligned} \frac{dx}{d\tau} &= \frac{\partial h}{\partial p_x} = 2t(\sin p_x - i\delta_x \cos p_x), \\ \frac{dy}{d\tau} &= \frac{\partial h}{\partial p_y} = 2t \sin(p_y - Bx), \\ \frac{dp_x}{d\tau} &= -\frac{\partial h}{\partial x} = 2Bt \sin(p_y - Bx), \\ \frac{dp_y}{d\tau} &= -\frac{\partial h}{\partial y} = 0. \end{aligned} \quad (\text{S.4})$$

One can obtain the coordinate functions and trajectories of the wave packet with given initial conditions of the coordinates and canonical momenta. In general, the above differential equations can only be solved numerically.

We are mainly interested in the long-wavelength limit, where expanding $E(\mathbf{k})$ around $(k_x, k_y) = (0, 0)$ yields $\varepsilon(\mathbf{k}) = t(k_x^2 + k_y^2) + 2i\delta_x k_x$. Accordingly, Eq. (S.4) reduce to

$$\begin{aligned}
\frac{dx}{d\tau} &= 2(tp_x - i\delta_x), \\
\frac{dy}{d\tau} &= 2t(p_y - Bx), \\
\frac{dp_x}{d\tau} &= 2Bt(p_y - Bx), \\
\frac{dp_y}{d\tau} &= 0,
\end{aligned} \tag{S.5}$$

which can be solved analytically. By eliminating the momenta in Eq. (S.5) we obtain the differential equations solely for the coordinates as

$$\begin{aligned}
\frac{d^2x}{d\tau^2} &= 2Bt \frac{dy}{d\tau}, \\
\frac{d^2y}{d\tau^2} &= -2Bt \frac{dx}{d\tau}.
\end{aligned} \tag{S.6}$$

The solutions of Eq. (S.6) have the form of

$$\begin{aligned}
x(\tau) &= A_1 e^{i\omega\tau} + A_2 e^{-i\omega\tau} + x_0, \\
y(\tau) &= i(A_1 e^{i\omega\tau} - A_2 e^{-i\omega\tau}) + y_0,
\end{aligned} \tag{S.7}$$

where $\omega = 2Btq/\hbar^2$ is the cyclotron frequency and the four parameters are determined by the initial conditions for the coordinates $x(0), y(0)$ and those for the momenta $p_x(0), p_y(0)$ through

$$\begin{aligned}
A_1 &= \frac{t[Bx(0) - ip_x(0) - p_y(0)] - \delta_x}{2Bt}, \\
A_2 &= \frac{t[Bx(0) + ip_x(0) - p_y(0)] + \delta_x}{2Bt}, \\
x_0 &= p_y(0)/B, \quad y_0 = y(0) - \frac{tp_x(0) - i\delta_x}{Bt}.
\end{aligned} \tag{S.8}$$

The periodic functions in Eq. (S.7) imply that a wave packet always forms closed orbits in the complex x - y space. Specifically, the projections of the trajectories in the $\text{Re}(x)$ - $\text{Re}(y)$ and $\text{Im}(x)$ - $\text{Im}(y)$ planes are closed loops described by the equations as

$$\begin{aligned}
\text{Re} : \left[x - \frac{p_y(0)}{B} \right]^2 + \left[y - y(0) + \frac{p_x(0)}{B} \right]^2 &= \left(\frac{A}{B} \right)^2, \\
\text{Im} : x^2 + \left(y - \frac{\delta_x}{Bt} \right)^2 &= \left(\frac{\delta_x}{Bt} \right)^2,
\end{aligned} \tag{S.9}$$

where $A = \sqrt{[Bx(0) - p_y(0)]^2 + p_x(0)^2}$. The closed orbits of the wave packet under a magnetic field mean that the quantization rule must be maintained due to the single-valued nature of the wave functions, which determines the energy values. Here, it is just the Onsager-Lifshitz quantization rule

$$\oint \mathbf{p} \cdot d\mathbf{r} = \left(n + \frac{1}{2} \right) h. \tag{S.10}$$

From Eq. (S.5), the relations between canonical momenta and velocities are

$$\begin{aligned}
p_x &= \frac{1}{2t} \frac{dx}{d\tau} + \frac{i\delta_x}{t}, \\
p_y &= \frac{1}{2t} \frac{dy}{d\tau} + Bx.
\end{aligned} \tag{S.11}$$

By inserting Eq. (S.11) into $\varepsilon(\mathbf{p} - q\mathbf{A})$ we obtain the energy as

$$\varepsilon = \frac{1}{4t} \left[\left(\frac{dx}{d\tau} \right)^2 + \left(\frac{dy}{d\tau} \right)^2 \right] + \frac{\delta_x^2}{t} = \frac{\omega^2}{t} A_1 A_2 + \frac{\delta_x^2}{t}. \tag{S.12}$$

Meanwhile, inserting Eq. (S.11) into the integral of Eq. (S.10) yields

$$\oint \mathbf{p} \cdot d\mathbf{r} = \oint \mathbf{p} \cdot \frac{d\mathbf{r}}{d\tau} d\tau = \frac{2\pi\omega}{t} A_1 A_2 = \left(n + \frac{1}{2}\right)h. \quad (\text{S.13})$$

By combining Eqs. (S.12) and (S.13) we finally obtain the real Landau levels as

$$\varepsilon_n = \left(n + \frac{1}{2}\right)\hbar\omega + \frac{\delta_x^2}{t}, \quad (\text{S.14})$$

which deviates from the standard results of normal particles by a factor δ_x^2/t stemming from the nonreciprocity. We conclude that, in the long wave-length limit, the closed orbits of the wave packet impose the quantization rule, which preserves real Landau levels despite the nonreciprocity. In contrast, semiclassical orbits solved numerically by Eq. (S.4) are open lines beyond the long-wavelength limit, which are shown in Fig. 3(b) of the main text. As a result, the quantization rules break down and the spectra become complex.

B. Nonreciprocal honeycomb lattice

In this subsection, we derive the semiclassical trajectories of the wave packet on the nonreciprocal honeycomb lattice. Without a magnetic field, the Bloch Hamiltonian reads

$$H'(\mathbf{k}) = \sum_{k_x, k_y} \begin{pmatrix} 0 & t_x^+ e^{-i\mathbf{k} \cdot \Delta_1} + t e^{-i\mathbf{k} \cdot \Delta_2} + t e^{-i\mathbf{k} \cdot \Delta_3} \\ t_x^- e^{i\mathbf{k} \cdot \Delta_1} + t e^{i\mathbf{k} \cdot \Delta_2} + t e^{i\mathbf{k} \cdot \Delta_3} & 0 \end{pmatrix} c_{k_x, k_y}^\dagger c_{k_x, k_y}, \quad (\text{S.15})$$

where $\Delta_1 = (1, 0)$, $\Delta_2 = (-\frac{1}{2}, \frac{\sqrt{3}}{2})$, $\Delta_3 = (-\frac{1}{2}, -\frac{\sqrt{3}}{2})$. The conduction and valence bands possess the following dispersion

$$E'_\pm(\mathbf{k}) = \pm \sqrt{t^2 - \delta_x^2 + 4t^2 \cos^2 \frac{\sqrt{3}k_y}{2} + 4t^2 \cos \frac{3k_y}{2} \left(\cos \frac{3k_x}{2} - \frac{\delta_x}{t} \sin \frac{3k_x}{2} \right)}. \quad (\text{S.16})$$

We expand the expressions around two Dirac points $\mathbf{K} = (0, \frac{4\pi}{3\sqrt{3}})$, $\mathbf{K}' = (0, -\frac{4\pi}{3\sqrt{3}})$ to study the physics in the long-wavelength limit. The energies reduce to

$$\varepsilon'_\pm(\mathbf{k}) = \pm \frac{3t}{2} \sqrt{k_x^2 + k_y'^2 - \left(\frac{2\delta_x}{3t}\right)^2 + \frac{4i\delta_x}{3t} k_x}, \quad (\text{S.17})$$

where $k_y' = k_y - \frac{4\pi}{3\sqrt{3}}$ is measured from the Dirac points. For $\delta_x = 0$, Eq. (S.17) describes massless Dirac particles. The semiclassical Hamiltonian for the conduction band under a magnetic field is modified into

$$h' = t_0 \sqrt{\left(p_x + i\frac{\delta_x}{t_0}\right)^2 + (p_y - Bx)^2} = t_0 h_0, \quad (\text{S.18})$$

with $t_0 = 3t/2$ and $h_0 = \sqrt{(p_x + i\frac{\delta_x}{t_0})^2 + (p_y - Bx)^2}$. The Hamilton's canonical equations read

$$\begin{aligned} \frac{dx}{d\tau} &= t_0 \frac{(p_x + i\frac{\delta_x}{t_0})}{h_0}, \\ \frac{dy}{d\tau} &= t_0 \frac{(p_y - Bx)}{h_0}, \\ \frac{dp_x}{d\tau} &= t_0 \frac{B(p_y - Bx)}{h_0}, \\ \frac{dp_y}{d\tau} &= 0. \end{aligned} \quad (\text{S.19})$$

Eliminating the momenta in Eq. (S.19) we obtain the differential equations solely for the coordinates as

$$\begin{aligned}\frac{d^2x}{d\tau^2} &= B \frac{t_0}{h_0} \frac{dy}{d\tau}, \\ \frac{d^2y}{d\tau^2} &= -B \frac{t_0}{h_0} \frac{dx}{d\tau}.\end{aligned}\tag{S.20}$$

The solutions of Eq. (S.20) have the form of

$$\begin{aligned}x(\tau) &= A'_1 e^{i\omega'\tau} + A'_2 e^{-i\omega'\tau} + x'_0, \\ y(\tau) &= i(A'_1 e^{i\omega'\tau} - A'_2 e^{-i\omega'\tau}) + y'_0,\end{aligned}\tag{S.21}$$

where $\omega' = qBt_0^2/(\hbar^2 h_0)$ is the cyclotron frequency and the four parameters are determined by the initial conditions through

$$\begin{aligned}A'_1 &= \frac{t_0[Bx(0) - ip_x(0) - p_y(0)] + \delta_x}{2Bt_0}, \\ A'_2 &= \frac{t_0[Bx(0) + ip_x(0) - p_y(0)] - \delta_x}{2Bt_0}, \\ x'_0 &= p_y(0)/B, \quad y'_0 = y(0) - \frac{t_0 p_x(0) + i\delta_x}{Bt_0}.\end{aligned}\tag{S.22}$$

The coordinate functions possess the same form as those of the normal particles in Eq. (S.7) so that the trajectories form closed orbits as well. The projections of the trajectories in the $\text{Re}(x)$ - $\text{Re}(y)$ and $\text{Im}(x)$ - $\text{Im}(y)$ planes are closed loops described by the equations as

$$\begin{aligned}\text{Re} : \left[x - \frac{p_y(0)}{B} \right]^2 + \left[y - y(0) + \frac{p_x(0)}{B} \right]^2 &= \left(\frac{A}{B} \right)^2, \\ \text{Im} : x^2 + \left(y + \frac{\delta_x}{Bt_0} \right)^2 &= \left(\frac{\delta_x}{Bt_0} \right)^2,\end{aligned}\tag{S.23}$$

with $A = \sqrt{[Bx(0) - p_y(0)]^2 + p_x(0)^2}$; see Fig. S.4(a). The same results hold true for the valence band as well. Similarly, closed orbits impose the following Onsager-Lifshitz quantization rule as

$$\oint \mathbf{p} \cdot d\mathbf{r} = \left(n + \frac{1}{2} - \gamma \right) h,\tag{S.24}$$

in which the factor $\gamma = \frac{1}{2}$ is due to the Berry phase of the Dirac particles, different from the case of normal particles.

We will show that the quantization also gives rise to real Landau levels. From Eq. (S.19), we have

$$\begin{aligned}p_x &= \frac{h_0}{t_0} \frac{dx}{d\tau} - \frac{i\delta_x}{t_0}, \\ p_y &= \frac{h_0}{t_0} \frac{dy}{d\tau} + Bx.\end{aligned}\tag{S.25}$$

By inserting Eq. (S.25) into Eq. (S.18), the energy can be expressed as

$$\varepsilon'_{\pm} = \pm h_0 \sqrt{\left(\frac{dx}{d\tau} \right)^2 + \left(\frac{dy}{d\tau} \right)^2} = \pm 2h_0 \sqrt{A_1 A_2} \omega.\tag{S.26}$$

Meanwhile, inserting Eq. (S.25) into the integral in Eq. (S.24) yields

$$\oint \mathbf{p} \cdot d\mathbf{r} = \oint \mathbf{p} \cdot \frac{d\mathbf{r}}{d\tau} d\tau = \frac{2\pi\omega h_0}{t_0} 4A_1 A_2 = nh.\tag{S.27}$$

By combining Eqs. (S.26) and (S.27) we obtain the real Landau levels as

$$\varepsilon_n^D = \varepsilon'_{\pm n} = \pm \frac{3}{2} t \sqrt{q\hbar n B},\tag{S.28}$$

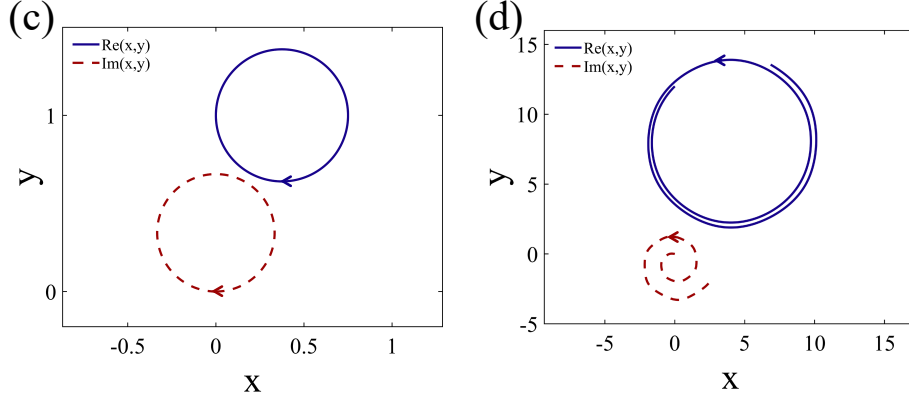


FIG. S.4: Projections of the semiclassical trajectories in the real and imaginary x - y planes for the nonreciprocal honeycomb lattice. (a) Closed orbits in the long-wavelength limit with $B = 0.4$, $x(0) = 0$, $y(0) = 1$, $p_x(0) = 0$, $p_y(0) = -0.15$, and (b) open trajectories beyond this limit with $B = 0.2$, $x(0) = 0$, $y(0) = 12$, $p_x(0) = 0.8$, $p_y(0) = 0.8$. Other parameter is $\delta_x = 0.2$.

which are just the familiar Landau levels for massless Dirac particles.

For more general cases, the Hamilton's canonical equations read

$$\begin{aligned}
 \frac{dx}{d\tau} &= \frac{3it \cos\left[\frac{\sqrt{3}(p_y - Bx)}{2}\right] e^{-\frac{3ip_x}{2}} (-t + e^{3ip_x}(t - \delta_x) - \delta_x)}{2E'_+(\mathbf{p} - q\mathbf{A})}, \\
 \frac{dy}{d\tau} &= -\frac{\sqrt{3}te^{-\frac{3ip_x}{2}} \sin\left[\frac{\sqrt{3}(p_y - Bx)}{2}\right] (t + e^{3ip_x}(t - \delta_x) + \delta_x + 4te^{\frac{3ip_x}{2}} \cos\left[\frac{\sqrt{3}(p_y - Bx)}{2}\right])}{2E'_+(\mathbf{p} - q\mathbf{A})}, \\
 \frac{dp_x}{d\tau} &= -\frac{\sqrt{3}Bte^{-\frac{3ip_x}{2}} \sin\left[\frac{\sqrt{3}(p_y - Bx)}{2}\right] (t + e^{3ip_x}(t - \delta_x) + \delta_x + 4te^{\frac{3ip_x}{2}} \cos\left[\frac{\sqrt{3}(p_y - Bx)}{2}\right])}{2E'_+(\mathbf{p} - q\mathbf{A})}, \\
 \frac{dp_y}{d\tau} &= 0,
 \end{aligned} \tag{S.29}$$

with $E'_+(\mathbf{p} - q\mathbf{A}) = \sqrt{t^2 - \delta_x^2 + 4t^2 \cos^2\left[\frac{\sqrt{3}(p_y - Bx)}{2}\right] + 4t^2 \cos\left[\frac{3(p_y - Bx)}{2}\right] \left(\cos\frac{3p_x}{2} - \frac{\delta_x}{t} \sin\frac{3p_x}{2}\right)}$. We solve these equations numerically and plot the semiclassical trajectories that are open lines in Fig. S.4(b). Therefore, the quantization conditions disappear and the energy spectra become complex beyond the long-wavelength limit.

IV. ENERGY SPECTRA OF NONRECIPROCAL SQUARE LATTICE UNDER x -OBC

Fig. S.5 shows the energy spectra for different strengths of the nonreciprocal hopping $\delta_x \in [0, 2t/5]$ under the x -OBC, where the in-gap streaks are edge states. The energy spectra are entirely real and exhibit a weak dependence on δ_x . Moreover, the Landau fan in the long-wavelength limit exhibits equal level spacing and linear dependence on B , which reduces to the behavior of free particles with a quadratic dispersion, the same as that under the x -PBC.

V. PROOF OF THE EXPONENTIAL PHASE BOUNDARY

We have seen in Fig. 4 of the main text that a \mathcal{MT} transition can be induced by both the boundary parameter γ_B and the magnetic field B for systems with a finite size in the x -direction. The critical phase boundary can always be well fitted by exponential functions. Here, we prove this result for $B = 0$. In this case, the Fourier transformed (y -direction) Hamiltonian reduces to

$$\tilde{H} = t_x^+ c_{m+1}^\dagger c_m + t_x^- c_m^\dagger c_{m+1} + 2tc_m^\dagger c_m + \gamma_B (t_x^+ c_1^\dagger c_M + t_x^- c_M^\dagger c_1), \tag{S.30}$$

where the original k_y dependent term that is irrelevant to the phase boundary has been dropped and the tunable boundary hopping is introduced.

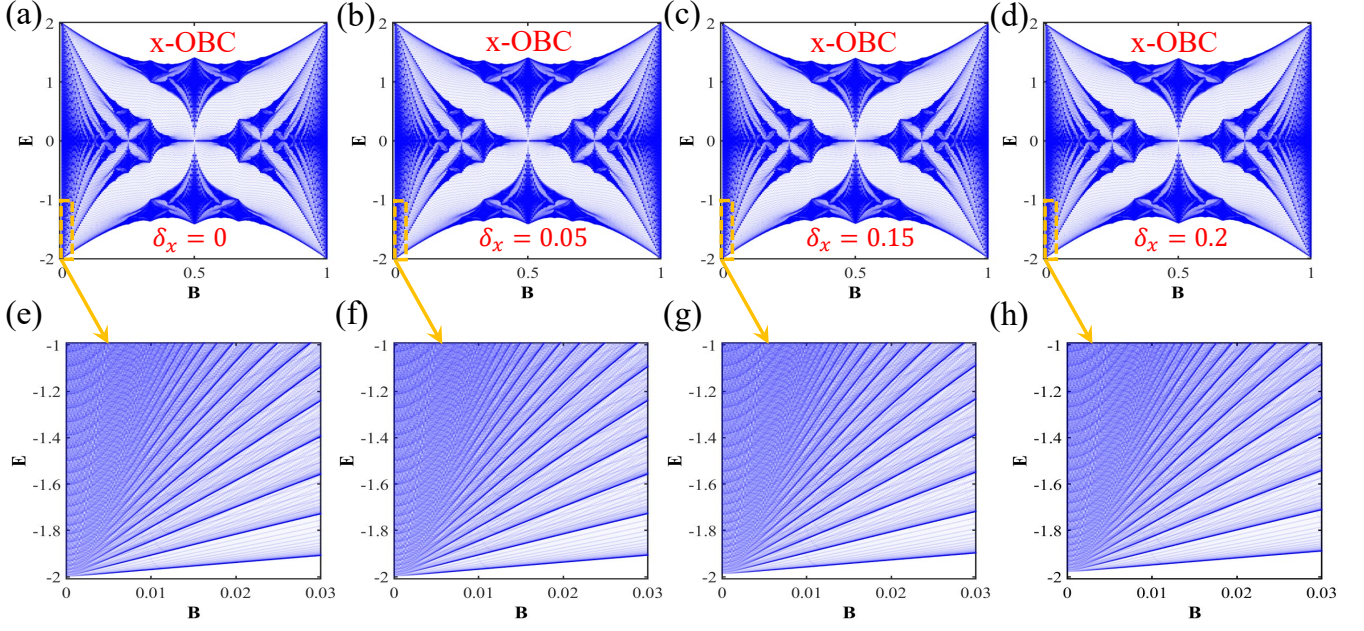


FIG. S.5: (a-d) Energy spectra under the x -OBC and y -PBC for $\delta_x = 0, 0.05, 0.15, 0.2$ with $M = 50$, $t = 0.5$. (e-h) Zoom of the Landau fan structures corresponding to (a-d).

The eigenvalue equation $\tilde{H}|\Psi\rangle = E|\Psi\rangle$ with $|\Psi\rangle = \sum_m \psi_m |m\rangle$ and $|m\rangle = c_m^\dagger |0\rangle$ ($m = 1, \dots, M$) consists of the bulk equations

$$t_x^+ \Psi_{j-1} - E \Psi_j + t_x^- \Psi_{j+1} = 0 \quad (\text{S.31})$$

with $j = 2, \dots, M-1$, and the boundary equations

$$\begin{aligned} -E \Psi_1 + t_x^- \Psi_2 + \gamma_B t_x^+ \Psi_M &= 0, \\ \gamma_B t_x^- \Psi_1 + t_x^+ \Psi_{M-1} - E \Psi_M &= 0. \end{aligned} \quad (\text{S.32})$$

Due to the spatially translational invariance of bulk equations, we can take the ansatz of wave function Ψ_i as:

$$\Psi_i = (\beta_i, \beta_i^2, \beta_i^3, \dots, \beta_i^{M-1}, \beta_i^M)^T. \quad (\text{S.33})$$

From Eq. (S.31) and Eq. (S.33), we obtain the eigenvalue in terms of β_i as

$$E = \frac{t_x^+}{\beta_i} + t_x^- \beta_i. \quad (\text{S.34})$$

For any E , there are two solutions $\beta_i = \beta_1, \beta_2$ that fulfill the constraint

$$\beta_1 \beta_2 = \frac{t_x^+}{t_x^-}. \quad (\text{S.35})$$

Note that any superposition of the two linearly independent solutions $\Psi = b_1 \Psi_1 + b_2 \Psi_2 = (\psi_1, \psi_2, \dots, \psi_M)$ is also a solution of Eq. (S.31), where $\psi_m = b_1 \beta_1^m + b_2 \beta_2^m$.

Inserting Ψ into the boundary equations yields

$$(\beta_1^{M+1} + \beta_2^{M+1}) - \left(\frac{t_x^+ \gamma_B^2}{t_x^-}\right) (\beta_1^{M-1} - \beta_2^{M-1}) - \left[1 + \left(\frac{t_x^+}{t_x^-}\right)^M\right] \gamma_B (\beta_1 - \beta_2) = 0. \quad (\text{S.36})$$

It is convenient to set the two solutions as

$$\beta_1 = r e^{i\theta}, \quad \beta_2 = r e^{-i\theta} \quad (\text{S.37})$$

with $r = \sqrt{t_x^+/t_x^-}$, which fulfills Eq. S.35. Then Eq. (S.36) reduces to

$$\sin[(M+1)\theta] - \eta_1 \sin[(M-1)\theta] - \eta_2 \sin \theta = 0, \quad (\text{S.38})$$

with $\eta_1 = \gamma_B^2$ and $\eta_2 = \gamma_B(r^{-M} + r^M)$, and the eigenvalues become

$$E = 2\sqrt{t_x^+ t_x^-} \cos \theta. \quad (\text{S.39})$$

The eigenvalue E may be real or complex depending on the solutions of θ in Eq. (S.38).

For $\gamma_B = 0$, i.e., the x -OBC, we have $\eta_1 = \eta_2 = 0$, Eq. (S.38) reduces to

$$\sin[(M+1)\theta] = 0, \quad (\text{S.40})$$

which yields M real roots as $\theta = l\pi/(M+1)$ with $l = 1, \dots, M$. As a result, the system is in the \mathcal{MT} -symmetric phase with entirely real energy spectra under the x -OBC.

For $\gamma_B \neq 0$, we rewrite Eq. (S.38) as $F_1(\theta) = F_2(\theta)$ with

$$F_1(\theta) = \sin[(M+1)\theta] - \eta_1 \sin[(M-1)\theta], \quad F_2(\theta) = \eta_2 \sin \theta. \quad (\text{S.41})$$

The eigenvalues E are determined by the solutions of $F_1(\theta) = F_2(\theta)$, which correspond to the crossing points of the two functions. It can be shown that as long as $\eta_2 < 1 + \eta_1$, there exist M real solutions for θ and E ; Otherwise, as $\eta_2 > 1 + \eta_1$, some of the solutions of θ and E become complex [70]. As a result, $\eta_2 = 1 + \eta_1$ gives the \mathcal{MT} transition point, which determines the critical value $\gamma_B^c = r^{-M}$ for $\gamma_B \leq 1$. The phase boundary possesses the asymptotic form for $\delta_x \ll t$ as

$$\gamma_B^c = e^{-\delta_x M/t}, \quad (\text{S.42})$$

showing that it is an exponential function.

VI. SIZE EFFECT OF THE \mathcal{MT} TRANSITION

Eq. (S.42) also tells that the function of the phase boundary $\gamma_B^c(\delta_x)$ strongly depends on the system size M in the x -direction. Specifically, the area of the \mathcal{MT} -symmetric phase reduces as M increases. In Fig. S.6, we plot the phase diagrams to show the size effect on the \mathcal{MT} phase transition. One can see that for $M = 200$ that is larger than $M = 50$ in the main text, the \mathcal{MT} -symmetric region undergoes a considerable shrinkage for both zero and finite magnetic field. Although the magnetic field has a smaller effect on the critical phase boundary compared with that for $M = 50$, it still results in a considerable reduction of the order parameter d_{HS} , which indicates that the magnetic field always increases the number of states with real energies, consistent with our discussion on the Onsager-Lifshitz quantization in the long-wavelength limit.

The size effect implies that no phase transition can occur as the system is infinitely large in the x -direction. However, realistic physical systems always possess a finite size and the boundary condition can also be continuously tuned in certain artificial systems such as the electrical circuits. Therefore, the \mathcal{MT} transition can be promisingly achieved by experiments.

VII. \mathcal{MT} -BREAKING BY NON-HERMITIAN COMPLEX HOPPING

In this section, we study the case that a small imaginary part $i\eta$ added to the hopping terms as $\tilde{t}_x^\pm = t + i\eta \pm \delta_x$, which yields a non-Hermitian complex hopping. Mathematically, this is just a substitution $t \rightarrow \tilde{t} = t + i\eta$ in the x -direction, which leads to entirely complex energy spectra including the energy levels in the long-wavelength limit; see Fig.S.7 for comparison. From the symmetry perspective, the additional $i\eta$ term breaks the \mathcal{MT} symmetry. As a result, the original \mathcal{MT} spectral transition disappears, which further verifies the \mathcal{MT} scenario in our work.

From Fig.S.7, one can see that the real and imaginary parts of the eigenvalues exhibit a linear relation in the long-wavelength limit (band edges), which can be solved analytically as

$$\tilde{\epsilon}_n = (n + 1/2)\hbar\tilde{\omega} + \delta_x^2/\tilde{t}, \quad (\text{S.43})$$

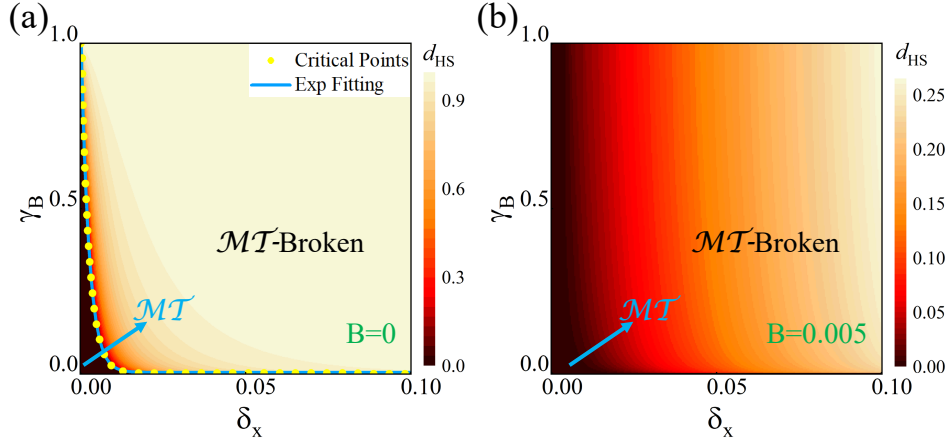


FIG. S.6: \mathcal{MT} phase diagram for $M = 200$. Other parameters are the same as those in Fig. 5 of the main text.

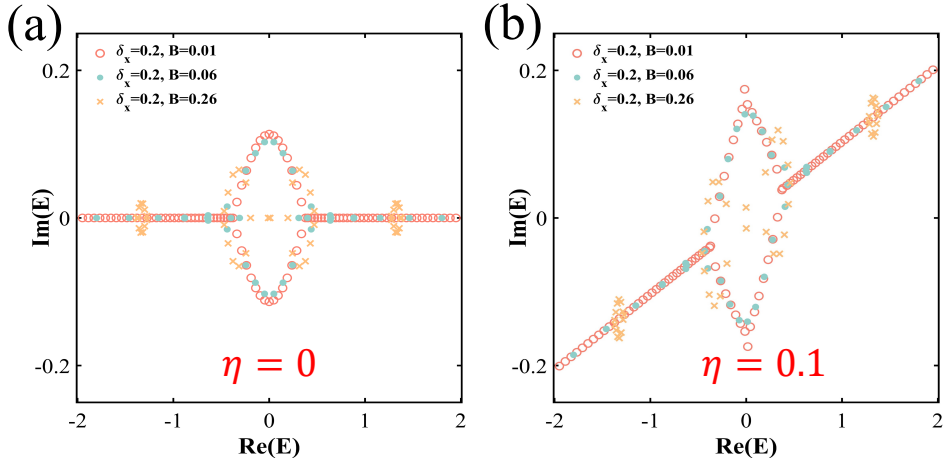


FIG. S.7: Complex energy spectra under different B with (a) $\eta = 0$ and (b) $\eta = 0.1$, respectively. Common conditions: x -PBC, y -PBC, $t = 0.5$ and $\delta_x = 0.2$.

where $\tilde{\omega} = qB/\sqrt{m_x m_y}$ becomes complex due to the complex effective mass $m_x = \hbar^2/(2\tilde{t}a^2)$ in the x -direction. Although the eigenvalues $\tilde{\varepsilon}_n$ become complex, the quantization persists. It is verified by the numerical results in Fig. R.5, in which the Landau fan structure of the real components still possesses equal level spacing and a linear B -dependence.

VIII. MAGNETIC ENERGY SPECTRA AND PHASE DIAGRAMS FOR NONRECIPROCAL HONEYCOMB LATTICE

From Eq. (S.1) and the Fourier transformed Hamiltonian \tilde{H}' , we plot the magnetic energy spectra in Fig. S.9 under both the x -OBC and x -PBC for the nonreciprocal honeycomb lattice. The spectra under the x -OBC are entirely real despite the nonreciprocity. In contrast, complex spectra are induced by the nonreciprocity under the x -PBC, where the fractal patterns merge into continuous pieces in the parametric regions far away from the long-wavelength limit. In the vicinity of the Dirac points, the same Landau fan structures arise for both the x -OBC and x -PBC; see Figs. S.9(a) and S.9(d). In particular, the quantized energy levels satisfy $E_n \propto \pm\sqrt{nB}$ with $n = 0, 1, \dots$; see Fig. S.9(b), manifesting the massless Dirac particle.

To study the \mathcal{MT} -symmetry breaking, we introduce a tunable boundary hopping, $\gamma_B(t_x^+ b_{1,n}^\dagger a_{M,n} + t_x^- a_{M,n}^\dagger b_{1,n})$, between the outmost sites $(1, n)_B$ and $(M, n)_A$, where $\gamma_B \in [0, 1]$ with $\gamma_B = 0$ and $\gamma_B = 1$ corresponding to the x -OBC and x -PBC, respectively. We calculate the order parameter d_{HS} using $\mathcal{MT}\psi_{a(b),i}^R(m, k_y) = \psi_{a(b),i}^{R*}(m, k_y)$ and plot the

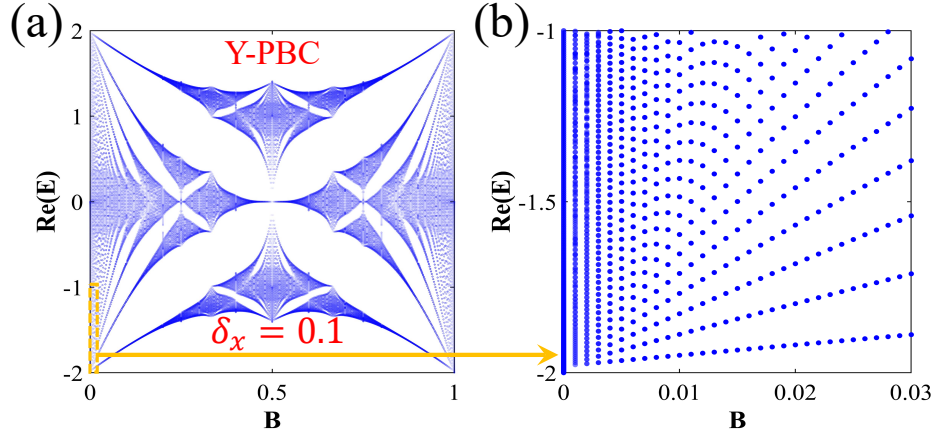


FIG. S.8: Energy spectra under x -PBC, y -PBC with $\delta_x = 0.1$, $\eta = 0.1$, $t = 0.5$, and $N = 50$.

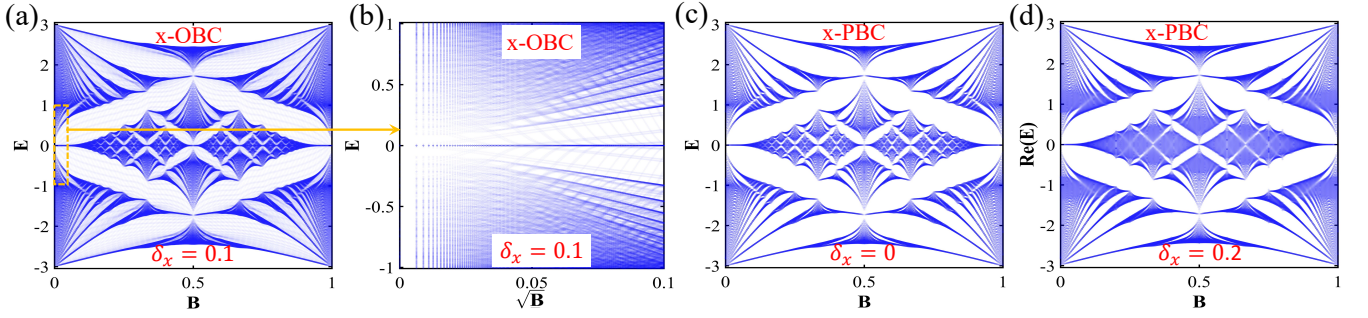


FIG. S.9: (a) Energy spectra under the x -OBC and y -PBC with $\delta_x = 0.1$ and $M = 100$. (b) Zoom of the Landau fan with the rescaled horizontal ordinate \sqrt{B} . Energy spectra under the x -PBC and y -PBC calculated in the momentum space (k_x, k_y) for (c) $\delta_x = 0$ and (d) $\delta_x = 0.2$. In all figures, $t = 1$.

phase diagrams in Fig. S.10. The phase diagrams resemble the main text fig(4) for the square lattice quite well, which reveals the universality of the spectral phase transition induced by spontaneously \mathcal{MT} -symmetry breaking, and a magnetic field can effectively suppress the \mathcal{MT} -symmetry breaking.

All the results in this section are consistent with those of the nonreciprocal square lattice.

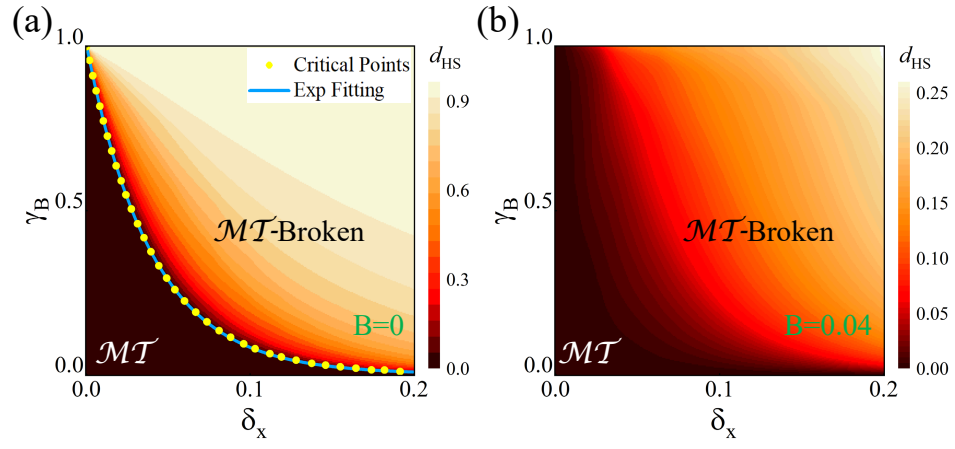


FIG. S.10: The order parameter d_{HS} as a function of δ_x and γ_B with (a) $B = 0$ and (b) $B = 0.04$. Critical points in (a) mark the real-to-complex spectral transition. The phase boundaries defined by the d_{HS} contours are fitted by the exponential functions. Other parameters are set as $M = 25$ and $t = 1$.